PHYSICAL REVIEW B **85**, 075406 (2012)

Carrier confinement in Ge/Si quantum dots grown with an intermediate ultrathin oxide layer

V. Kuryliuk
Department of Physics, Taras Shevchenko Kyiv National University, Kyiv 01601, Ukraine

O. Korotchenkov[*] and A. Cantarero
Materials Science Institute, University of Valencia, P. O. Box 22085, E-46071 Valencia, Spain
(Received 4 August 2011; revised manuscript received 30 December 2011; published 8 February 2012)

We present computational results for strain effects on charge carrier confinement in Ge_xSi_{1-x} quantum dots (QDs) grown on an oxidized Si surface. The strain and free carrier probability density distributions are obtained using the continuum elasticity theory and the effective-mass approximation implemented by a finite-element modeling scheme. Using realistic parameters and conditions for hemisphere and pyramid QDs, it is pointed out that an uncapped hemisphere dot deposited on the Si surface with an intermediate ultrathin oxide layer offers advantageous electron-hole separation distances with respect to a square-based pyramid grown directly on Si. The enhanced separation is associated with a larger electron localization depth in the Si substrate for uncapped hemisphere dots. Thus, for dot diameters smaller than 15–20 nm and surface density of the dots (n_{QD}) ranging from about 10^{10} to 10^{12} cm^{-2}, the localization depth may be enhanced from about 8 nm for a pyramid to 38 nm for a hemisphere dot. We find that the effect in a hemisphere dot is very sensitive to the dot density and size, whereas the localization depth is not significantly affected by the variation of the Ge fraction x in Ge_xSi_{1-x} and the aspect ratio of the dot. We also calculate the effect of the fixed oxide charge (Q_{ox}) with densities ranging from 10^{-9} to 10^{-7} C/cm^2 for 10-Ω cm p-type Si wafers on the carrier confinement. Although the confinement potential can be strongly perturbed by the charge at n_{QD} less than $\approx 4 \times 10^{11}$ cm^{-2}, it is not very sensitive to the value of Q_{ox} at higher n_{QD}. Since, to our knowledge, there are no data on carrier confinement for Ge QDs deposited on oxidized Si surfaces, these results might be applicable to functional devices utilizing separated electrons and holes such as photovoltaic devices, spin transistors, and quantum computing components. The use of hemisphere QDs placed on oxidized Si rather than pyramid dots grown on bare Si may help to confine charge carriers deeper inside the Ge/Si heterostructure in order to reduce the influence of surfaces and interfaces on transport properties of the structures.

DOI: 10.1103/PhysRevB.85.075406 PACS number(s): 62.25.−g, 73.21.La, 73.22.−f

I. INTRODUCTION

There has been a great interest in the preparation, characterization, and potential application of self-assembled quantum dots (QDs) over the past few decades. Most often, the dots have been overgrown with the matrix semiconductor and are not directly on the surface. Less well understood is the effect of uncapped QDs on the electronic properties of the subsurface region. This region is altered importantly because a part of the surface is composed of the dot material rather than the matrix, and therefore a strong strain field is added.

Strain is a fundamental issue in semiconductor heterostructures. In particular, heterostructures on Ge/Si allow both band gap and strain engineering using silicon technology.[1,2] Strain influences the band structure by (1) imposing the crystal lattice volume change, which shifts positions of energy bands, and (2) lowering the crystal symmetry, which splits degeneracies in bands. With carefully engineered strain, it is possible to achieve a desired band offset between different materials, create local confinement and periodic band-gap modulation, improve charge carrier mobilities by eliminating low-mobility channels, or reducing scattering via lowering the band degeneracy.[1,3–8]

The possibility to tailor the mechanical and electronic properties of semiconductor QD structures with strains renders this research field interesting for several important technological fields. Germanium QDs grown on (or embedded in) silicon have been successfully employed in solar cells[9,10] and in electronic[11] and optoelectronic devices[12] due to their simplicity in the band-gap engineering and compatibility with Si-based integrated electronics. Ge/Si nanostructures with long coherence times of free carriers are also promising for spintronic applications.[13–15] Application of strain-induced effects to single Ge QD devices has recently been achieved. In particular, the first example of a single-hole supercurrent transistor based on SiGe has been successfully demonstrated.[16] The applicability of strains originating from SiGe QDs for the mobility enhancement in n-channel metal-oxide-semiconductor field-effect transistors (MOSFETs) has also been experimentally demonstrated.[17]

Recently, Ge nanodots deposited on oxidized Si have become the subject of increasing interest with a perspective of future pathways and potential new applications in the current Si-based technology, including advanced silicon photonics and oxide-on-silicon capacitors.[18–23] With this technique, sphere-shaped dots only contact the Si substrate through nanometer-sized voids resulting in epitaxial growth of elastically strain-relaxed QDs without misfit dislocations. The main advantage of these techniques is that they provide a nearly uniform and tunable size distribution, allowing us to achieve a dot density (n_{QD}) as high as 10^{12} cm^{-2}. Both uncapped dots[22,24] and dots buried in Si (Ref. 25) have been realized on oxidized Si surfaces.

Many theoretical studies have been carried out to investigate the strain distributions around quantum dots. The computation

 ©2012 American Physical Society

of strains has been performed either analytically or numerically in a number of cases of practical relevance. Finite-element method[26,27] (FEM) and Green's function techniques[28–33] have been systematically employed. Strain gives rise to a deformation potential around the dots, which affects the electronic structure and thus the basic electrical and optical properties of QD structures. The strain itself is particularly important since it is used as input in efficient semiempirical approaches to electronic-structure calculations, such as $\boldsymbol{k} \cdot \boldsymbol{p}$, empirical pseudopotential, or tight-binding methods.[34–38] The effect of strain on the electronic properties of Ge_xSi_{1-x} QDs grown on oxidized Si surfaces are, however, little known. This, of course, is not favorable for experiments and applications in strained semiconductor devices.

In this work, we study the effect of strain on charge carrier confinement for uncapped and buried Ge_xSi_{1-x} dots with realistic structural and compositional parameters grown on oxidized Si wafer surfaces. Numerical calculations are performed for infinite arrays of quantum dots using the continuum elasticity theory implemented by a finite-element modeling scheme. These results can be used in a number of ways. Possible strategies involve confining charge carriers deeper inside a Ge/Si heterostructure to reduce the influence of surfaces and interfaces on the electrical properties and separating photogenerated electrons and holes in the strain fields developed at oxidized Ge/Si interfaces able to improve photovoltage performance of Ge/Si nanostructures. The results described in this work should also be applicable to functional devices utilizing electron and hole spins because increasing electron-hole separation distance can lead to decreasing exchange interaction between the electron and hole spins, thus providing enhanced spin coherence times and offering an important step toward the realization of spin transistors and quantum computing components.

II. DETERMINATION OF THE STRUCTURE

We compare two different elementary structures, a hemisphere Ge_xSi_{1-x} dot placed on an oxidized Si(001) surface and a square-based pyramid grown on bare Si(001), either uncapped or buried in Si. The structures are pseudomorphic with abrupt interfaces between Si and Ge_xSi_{1-x}, when the lattice mismatch strain is accommodated elastically without plastic relaxation via misfit dislocations or stacking faults.

In many cases, the size distribution of hemisphere Ge dots deposited on ultrathin SiO_2 films is rather narrow, with a mean diameter of 5–10 nm and a height of 2–3 nm,[18,23] providing a small aspect ratio (AR = height/base) varying between 0.2 and 0.6. As the growth temperature increases from about 300 °C to 500 °C, n_{QD} decreases from $\approx 4\times10^{12}$ to 2×10^{12} cm^{-2} while the lateral diameter increases from ≈2 to 10 nm.[39] On the other hand, two-dimensional arrays of Ge QDs with a periodicity of about 40 nm ($n_{QD} \approx 6\times10^{10}$ cm^{-2}) and an average dot diameter of 25 nm have been achieved by a selective growth in holes fabricated in thick SiO_2 films by the block copolymer patterning technique.[40,41] Furthermore, using the ultrathin SiO_2 film technique and a patterning technique yields nanoarrays of high-quality epitaxial QDs having a diameter of about 10 nm and separated by ≈25 nm ($n_{QD} \approx 2\times10^{11}$ cm^{-2}).[42] Therefore, in a realistic case, ensemble of hemispherical Ge dots may be described by the lateral size and surface density ranging from 5 to 25 nm and from 10^{10} to 4×10^{12} cm^{-2}, respectively.

In Ge dots grown on bare Si(001) by molecular beam epitaxy (MBE), a bimodal distribution of Ge QDs with multifaceted domes and square-based pyramids is commonly observed.[43] The base side of a pyramid is typically greater than 20–40 nm, while its AR is 0.1–0.15.[44]

An important problem connected with the growth of self-assembled dots is the intermixing between Ge dots and their neighborhood during growth[45–47] and overgrowth,[48,49] determining the vertical composition profile of uncapped and buried dots. Obviously, nominally pure Ge domes on Si(001) are intermixed already after growth, with a Ge content increasing from the dot base to the apex. Depending on the growth temperature, the maximum Ge concentration in a Ge_xSi_{1-x} alloy can reach values ranging from 70% to 100%, while the Ge content at the dots base is usually around 30%–50%. During overgrowth at temperatures above 600 °C, the maximum value drastically decreases down to about 40%. If domes are covered by a low-Ge concentration layer, their shape and high-Ge content can be preserved.

However, direct evidence of the real Ge concentration in QDs deposited on SiO_2 is still lacking. We address this issue here by using Raman scattering to analyze the optical phonon region and extract the Ge content in the hemisphere QDs studied in this work.

The growth of uncapped Ge_xSi_{1-x} QDs on the oxidized (001)-oriented *p*-Si wafer surface was performed by MBE within the scheme proposed by Shklyaev and Ichikawa.[20] In order to distinguish between the Raman lines arising from the substrate and those from the QD layer, we also analyzed strained uncovered Ge_xSi_{1-x} layers under the same experimental conditions. These were grown on (100) Si substrates by a combination of rapid thermal processing and chemical vapor deposition (RTCVD), resulting in 100-nm-thick strained $Ge_{0.25}Si_{0.75}$ layers. The growth procedure is described elsewhere (see, e.g., Dutartre *et al.*[50]).

Raman scattering measurements were carried out in backscattering geometry with a JobinYvon T64000 triple spectrometer equipped with a confocal microscope and a nitrogen-cooled charge-coupled device detector. A 100× microscope objective was used to focus the light to a 1-μm spot on the sample surface and collect the scattered signal to the spectrometer. The samples were excited with the 514.5-nm line of an Ar^+ laser. To minimize sample heating effects on the Raman spectra,[51] the power on the sample surface was set to 1–2 mW. This excitation produced no detectable sample heating as observed in the variation of the Raman frequencies and linewidths with changing power. Reference samples were prepared from Si(001) wafers used for Ge deposition. At a wavelength of about 500 nm, the optical absorption coefficient of Si is $\alpha \approx 18.5\times10^3$ cm^{-1},[52] and the light penetration depth, which is tested in Raman measurements, $1/2\alpha \approx 270$ nm. Raman spectra were recorded at room temperature.

Figure 1 shows Raman spectra of Ge_xSi_{1-x} QDs (spectrum 1) and a Si reference sample (spectrum 2). In accordance with previous results from bulk silicon, the substrate spectrum consists of three peaks at 225, 302, and 435 cm^{-1} in the region of interest, which originate from the two-phonon scattering of

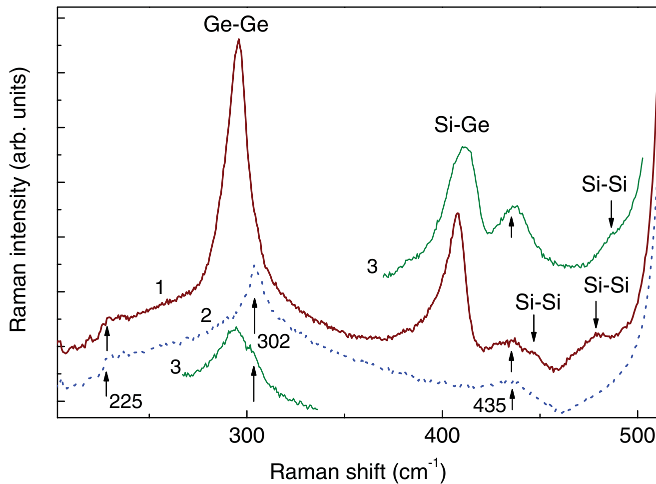

FIG. 1. (Color online) Raman spectra of uncapped Ge_xSi_{1-x} QDs, epitaxially grown on oxidized Si with no capping layer (spectrum 1) and a Si reference sample (spectrum 2). Spectrum 3, arbitrary shifted in vertical direction for the Ge-Ge and higher-wave-number ranges, corresponds to a 100-nm-thick $Ge_{0.25}Si_{0.75}$ layer.

2TA(L), 2TA(X), and 2TA(Σ), respectively.[53] It is well known that some spectral lines in the Raman spectrum of Ge_xSi_{1-x} dots grown on Si are related to the Si substrate, complicating the interpretation of the measurements.[54] Si substrate peaks appear at ≈225 and 435 cm^{-1} in spectrum 1 of the QD sample but seemingly broadened and slightly shifted to lower wave numbers compared to those in spectrum 2. Most generally, epitaxial growth of a lattice-mismatched system leads to the built-in strains. The strain originated from the lattice mismatch induces a shift of phonon energies. For example, in the case of in-plane $S_\parallel$ strain, the phonon frequency shift is given by $\Delta\omega = bS_\parallel$, where b is the phonon strain-shift coefficient or phonon deformation potential.[55] Since the lattice constant of SiGe is larger than that of Si, irrespective of the alloy composition, and $b < 0$,[56] Ge_xSi_{1-x} is compressed ($S_\parallel < 0$). In contrast, a tensile strain with $S_\parallel > 0$ is introduced in the Si substrate, resulting in lower phonon frequencies with $\Delta\omega < 0$. The Raman peak broadening and shift to lower wave numbers can at least in part explain the fact that the substrate peak at 302 cm^{-1} is smeared in spectrum 1 of Fig. 1 and disappears on the higher-wave-number side of a stronger Ge-Ge peak at about 297 cm^{-1}.[57–59] This is more clearly illustrated by examining the Ge-Ge peak in the $Ge_{0.25}Si_{0.75}$ layer (spectrum 3 in Fig. 1), which is composed of the overlapping Ge-Ge optic phonon and Si substrate acoustic phonon modes.

The absence of the substrate mode at about 300 cm^{-1} in spectrum 1 of Fig. 1 can also be merely explained by the fact that the energy of the laser line (2.41 eV) is in resonance with the electronic level ($E_1 + \Delta_1$) of the Ge_xSi_{1-x} alloy.[60,61] The Ge-Ge phonon mode has been found to exhibit a strong enhancement in the energy range from ≈2.2 to 2.6 eV,[61] thus decreasing the light penetration depth.

It is also evident from spectra 1 and 3 in Fig. 1 that there are distinct peaks centered near 410 cm^{-1}, which are due the scattering from optic phonons involving Si-Ge vibrations.[57–59] There are also weak structures at 447 and 479 cm^{-1} in spectrum 1, and a weak peak centered near 486 cm^{-1} in spectrum 3. These additional peaks, observed between 420 and 500 cm^{-1}, have been attributed to either the localized Si-Si motion in the neighborhood of one or more Ge atoms[62] or to a long-range ordering in strained epitaxial layers SiGe/Si.[63] The frequencies of the localized Si-Si modes are lowered with respect to a Si substrate peak at about 520 cm^{-1} because of the large mass of neighboring Ge atoms.

The principal conclusion from the experimental results is therefore that the peak positions of the Ge-Ge and Si-Ge vibrations can be determined precisely since most Raman signals at these positions are from the Ge_xSi_{1-x}-related vibration modes. It is seen that the Si-Si mode is rather weak in spectrum 1 of Fig. 1, as expected for a Ge-reach alloy in the dot. The frequencies of the other two, $\omega_{\text{Ge-Ge}}$ and $\omega_{\text{Si-Ge}}$, can be fitted via varying the Ge fraction x and strain as follows[64]:

$$\omega_{\text{Ge-Ge}} = 284 + 5x + 12x^2 + b_{\text{Ge-Ge}}\langle S_\parallel\rangle, \quad (1)$$

$$\omega_{\text{Si-Ge}} = 400 + 29x - 95x^2 + 213x^3 - 170x^4 + b_{\text{Si-Ge}}\langle S_\parallel\rangle, \quad (2)$$

where $\langle S_\parallel\rangle$ is the average in-plane strain, $b_{\text{Ge-Ge}}$ is the phonon strain-shift coefficient for the Ge-Ge mode, and $b_{\text{Si-Ge}}$ is that for the Si-Ge mode.

Taking $b_{\text{Ge-Ge}} = -400$ cm^{-1}, $b_{\text{Si-Ge}} = -575$ cm^{-1},[65,66] and using $\omega_{\text{Ge-Ge}} = 297.4$ cm^{-1}, $\omega_{\text{Si-Ge}} = 409.7$ cm^{-1} deduced from Fig. 1 yields $x = 0.73$ and $\langle S_\parallel\rangle = -0.82\%$.

In a larger set of experimental samples, the value of x ranged from 0.72 to 0.91. From this consideration, it follows that the strains and carrier confinement effects in oxidized Ge_xSi_{1-x}/Si QD structures can be characterized fully by varying x from 0.7 to 1.

III. COMPUTATIONAL DETAILS

We have carried out computations for a system composed of a periodically repeated unit cell shown in Fig. 2. Consider hemisphere Ge_xSi_{1-x} dots with height H and a base diameter D. The interdot distance is L_{ID}. According to recent transmission electron microscopy results, Si oxide film remains under Ge_xSi_{1-x} nanocrystals, but ultrasmall voids with a size below 1 nm are formed in the film just under the nanocrystals, thus allowing them to grow epitaxially on the Si substrate.[42] Based on this finding, we assume that the dot on oxidized Si is modeled as a crossover of two primitive shapes, including a hemisphere and a cylinder neck of diameter d, which is spacing between a Ge_xSi_{1-x} dot and the substrate. In our calculations, the dots are either uncovered by a cap layer or covered by a Si cap with a thickness of up to 10 times greater than the height of the dot.

To determine the distribution of the electron and hole wave functions in the strain field induced by QDs, the two-dimensional (2D) steady-state effective-mass Schrödinger equation can be written as

$$\left(-\frac{\hbar^2}{2m_\parallel^{e,h}}\frac{\partial^2}{\partial y^2} - \frac{\hbar^2}{2m_\perp^{e,h}}\frac{\partial^2}{\partial z^2}\right)\Psi^{e,h}(y,z) + U^{e,h}(y,z)\,\Psi^{e,h}(y,z) = E^{e,h}\Psi^{e,h}(y,z), \quad (3)$$

where $m_\perp^{e,h}$ and $m_\parallel^{e,h}$ are the effective masses in the growth and lateral directions, respectively, $\Psi^{e,h}(y,z)$ and $E^{e,h}$ are

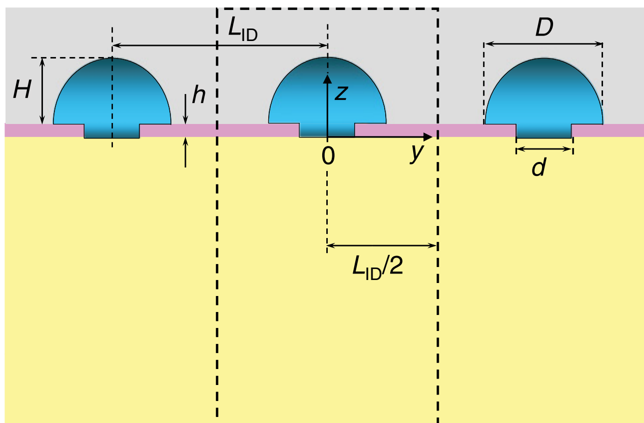

FIG. 2. (Color online) Geometry of the problem including three unit cells of epitaxially grown hemisphere Ge_xSi_{1-x} dots (height H and base diameter D) grown on (001)-oriented Si substrate with an intermediate SiO_2 layer of thickness h and a cylinder neck of diameter d between the QD and the substrate. The z axis is the [001] crystal direction.

the electron (e) and hole (h) wave functions and energies, respectively, $U^e(y,z)$ and $U^h(y,z)$ are the confinement potentials of electrons and holes, which are the sum of the carrier confinement in the dot potential and the strain-induced carrier confinement, i.e.,

$$U^e(y,z) = \triangle E_C + a_c S_h(y,z) + \frac{\triangle_0}{3} + \frac{b_c S_b(y,z)}{3}, \quad (4)$$

$$U^h(y,z) = \triangle E_V + a_v S_h(y,z) + \frac{\triangle_0}{3} - \frac{b_v S_b(y,z)}{2}, \quad (5)$$

where $\triangle E_C$ and $\triangle E_V$ are the conduction- and valence-band offsets, a_c and a_v are the hydrostatic deformation potentials for the conduction and valence bands, respectively, b_v is the corresponding shear deformation potential, b_c is the deformation potential at the Δ point of the conduction-band valley, $\triangle_0$ is the spin-orbit splitting, and S_h and S_b are the hydrostatic and biaxial strains, respectively. In accordance with linear elasticity, we can write

$$T_{ij}(y,z) = C_{ijkl}[S_{kl}(y,z) - S_{0kl}(y,z)], \quad (6)$$

where T_{ij} is the stress tensor, C_{ijkl} is the elastic module tensor, S_{kl} is the strain tensor, and $S_{0kl}(y,z)$ are the components of the initial strain tensor due to a lattice mismatch. The initial strain is assumed nonvanishing only inside the dot and can be calculated from the lattice parameters in the dots (a_i) and the Si substrate (a_m) as follows:

$$S_{0kl}(y,z) = \frac{a_m - a_i}{a_m}\delta_{kl}, \quad (7)$$

where δ is the Kronecker delta.

We notice that the contracted notations $11\to 1$, $22\to 2$, $33\to 3, 23\to 4, 13\to 5, 12\to 6$ can be used for elastic module indexes ij and kl. Then, taking into account a cubic crystal structure of Si and Ge, the C_{ijkl} tensor can be given in terms of three independent components $C_{1111} = C_{11}$, $C_{1122} = C_{12}$, and $C_{2323} = C_{44}$.[67] In the isotropic SiO_2 material, the elastic module tensor has two independent components C_{11} and C_{12}, whereas $C_{44} = (C_{11} - C_{12})/2$.

In modeling an infinite array of quantum dots, composed of a periodically repeated unit cell, we apply a periodic boundary condition on the left- and right-hand sides of the unit cell (dotted-line rectangle in Fig. 2). With respect to a coordinate system introduced in Fig. 2, this condition is given by

$$u_y|_{y=-L_{ID}/2} = u_y|_{y=L_{ID}/2} = 0, \quad (8)$$

where u_y is the elastic displacement component.

Next, along all the external boundaries, including the open surface of an uncapped QD and the top surface of substrate excluding the part covered by an uncapped dot, the traction-free condition is imposed, i.e.,

$$T_{ij}n_j = 0 \quad (9)$$

with n_j the j component of the unit vector normal to the boundary and summation over $j = 1,2$.

Furthermore, in solving Eq. (6), the continuity conditions of mechanical displacement and traction are imposed across interfaces, including Ge_xSi_{1-x}-Si, Ge_xSi_{1-x}-SiO_2, and Si-SiO_2 interfaces, i.e.,

$$u_i\big|_{z=0}^{\mathrm{I}} = u_i\big|_{z=0}^{\mathrm{II}}, u_i\big|_{z=0}^{\mathrm{I}} = u_i\big|_{z=0}^{\mathrm{III}}, u_i\big|_{z=0}^{\mathrm{II}} = u_i\big|_{z=0}^{\mathrm{III}}, \quad (10)$$

$$T_{ij}n_j\big|_{z=0}^{\mathrm{I}} = T_{ij}n_j\big|_{z=0}^{\mathrm{II}}, T_{ij}n_j\big|_{z=0}^{\mathrm{I}} = T_{ij}n_j\big|_{z=0}^{\mathrm{III}},$$
$$T_{ij}n_j\big|_{z=0}^{\mathrm{II}} = T_{ij}n_j\big|_{z=0}^{\mathrm{III}}, \quad (11)$$

where superscripts I, II, and III refer to the substrate, dot, and oxide layer, respectively, and u_i is referred to as the u_y and u_z displacement components.

Finally, the condition of a rigid boundary is imposed on the bottom surface of the cell (at $z = -L_z$) shown in Fig. 2. This reflects the fact that the thickness of the area of interest near the Ge_xSi_{1-x}-Si interface is much less than the substrate thickness. Then,

$$u_y|_{z=-L_z} = u_z|_{z=-L_z} = 0. \quad (12)$$

The strain is computed from Eq. (6) using finite elements[68] (quadratic triangular elements with six nodes). Finer meshes are used inside the dot and near the interface. The FEM solution is produced for meshes with about 20 000 nodes with two degrees of freedom per node. Equation (3) is also solved using the FEM and the same mesh as for the strain is used. This gives rise to a sparse matrix and the computation is performed using standard solvers for sparse systems.

The general solution to Eq. (3) is then expressed as a linear combination of shape functions $\xi_i^{e,h}(y,z)$, i.e.,

$$\Psi^{e,h}(y,z) = \sum_{i=1}^{6} \varphi_i^{e,h}\xi_i^{e,h}(y,z). \quad (13)$$

We choose the shape functions to be second-order polynomials that have the value 1 in an ith single node of the mesh and 0 in other nodes. Substitution in Eq. (3) gives us

$$[H^{e,h}][\varphi^{e,h}] = E^{e,h}[M^{e,h}][\varphi^{e,h}], \quad (14)$$

TABLE I. Material parameters used in the calculations.

	Si	Ge	SiO_2
Lattice parameters[a] (Å)	5.43	5.65	
Elastic constants[b] (GPa)			
C_{11}	165.7	128.9	85.9
C_{12}	63.9	48.3	17.6
C_{44}	79.6	67.1	34.2
Effective masses[c,d]			
$m_{e\perp}/m_0$	0.98	1.6	0.5
$m_{e\parallel}/m_0$	0.19	0.08	0.5
$m_{h\perp}/m_0$	0.49	0.33	5.0
$m_{h\parallel}/m_0$	0.49	0.33	5.0
Electron deformation potential constants[a] (eV)			
a_c	4.18	−1.54	
a_v	2.46	1.24	
b_v	−2.35	−2.55	
b_c	9.16	9.42	
Δ_0	0.04	0.3	

[a]Reference 70.
[b]Reference 71.
[c]Reference 72.
[d]Reference 73.

where the matrix components are given by

$$H_{ij}^{e,h} = \frac{\hbar^2}{2}\int_{S_e}\frac{1}{m_{\parallel}^{e,h}}\frac{\partial\xi_i^{e,h}}{\partial y}\frac{\partial\xi_j^{e,h}}{\partial y}dy\,dz + \frac{\hbar^2}{2}\int_{S_e}\frac{1}{m_{\perp}^{e,h}}\frac{\partial\xi_i^{e,h}}{\partial z}\frac{\partial\xi_j^{e,h}}{\partial z}dy\,dz + \int_{S_e}U^{e,h}\xi_i^{e,h}\xi_j^{e,h}dy\,dz \tag{15}$$

and

$$M_{ij}^{e,h} = \int_{S_e}\xi_i^{e,h}\xi_j^{e,h}dy\,dz. \tag{16}$$

In Eqs. (15) and (16), the integration extends over the surface area S_e of the finite element.

Our approach to solving the eigenvalue problem given by Eq. (14) exploits the FEAST algorithm.[69] In Table I, we give an overview of the numerical parameters used in the calculations. The values for a Ge_xSi_{1-x} alloy are calculated by linear interpolation from the respective values for Ge and Si.

IV. RESULTS AND DISCUSSION

A. Strain distribution

The principal results of the strain variation for an uncapped hemisphere Ge_xSi_{1-x} dot are summarized in Fig. 3. The strain components are plotted for the middle cross section of the dot. The modeled dot is hemisphere shaped with height $H = 2.5$ nm and a base diameter $D = 7$ nm, similar to experimentally available dots described above. In this calculation, a 0.3-nm-thick SiO_2 layer is used with a 1-nm-diameter neck connecting the QD and the substrate (see Fig. 2).

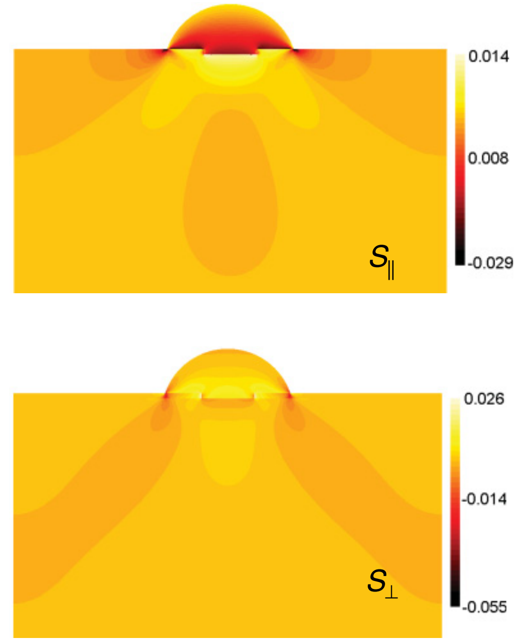

FIG. 3. (Color online) Strain distribution at a middle cross-sectional [001]-[010] plane (24 × 25 nm^2 in size), through the center of an uncapped hemisphere $Ge_{0.73}Si_{0.27}$/Si dot. $S_\parallel$ is the in-plane strain equal to S_{11}, whereas the out-of-plane strain $S_\perp$ is S_{22}. The negative and positive strain values correspond to compressive and tensile strains, respectively. The interdot distance $L_{ID} = 24$ nm, corresponding to the dot density of 1.7×10^{11} cm^{-2}.

It is apparent that the bottom layer of a Ge_xSi_{1-x} dot is compressed parallel to the interface since the in-plane lattice constant of the dot material is forced to be equal to that of the substrate. Due to a greater lattice constant of Ge compared to that of Si, the compressive interfacial strain (negative $S_\parallel$ above the interface in Fig. 3) causes an expansion along the z direction, due to a Poisson effect. This results in positive $S_\perp$ values within the QD. Consistent with this qualitative picture, both $S_\parallel$ and $S_\perp$ components are positive in outer layers of a hemisphere dot.

It is obvious that the character of the strain and effects of strain on charge carrier confinement are not determined by the separate components of the strain tensor, but by decomposing it into the hydrostatic and shear strain components. Thus, the shift of the conduction-band extremum can be expressed in terms of strains and deformation potentials as

$$\delta E_C = a_c S_h + (b_c/3) S_b \tag{17}$$

with $S_h = 2S_\parallel + S_\perp$ and $S_b = 2(S_\perp - S_\parallel)$. The conduction-band shift is then given by

$$\delta E_C = \left(2a_c - \frac{2b_c}{3}\right) S_\parallel + \left(a_c + \frac{2b_c}{3}\right) S_\perp. \tag{18}$$

From the values of a_c and b_c given in Table I, we find that δE_C is much more affected by the $S_\perp$ strain component than by $S_\parallel$.

We can now try to bring theory into agreement with experiment using the strain estimates given in Sec. II. Clearly, the calculated strain distributions displayed in Fig. 3 may not be directly compared to Raman data for Ge_xSi_{1-x} shown in

Fig. 1. To make a comparison, the computed in-plane strain can be averaged over the cross-sectional area S of the dot according to

$$\langle S_\parallel \rangle = \frac{1}{S}\int_S S_\parallel(y,z)dy\,dz, \tag{19}$$

which yields $\langle S_\parallel \rangle = -0.79\%$. This is clearly in accord with the value $\langle S_\parallel \rangle = -0.82\%$ obtained from the Raman spectrum.

B. Electronic structure

The detailed spatial distribution of the electron wave functions for the lowest localized state, which is denoted by E_0 below, is shown in the left-hand images of Fig. 4 for uncapped hemisphere [Fig. 4(a)] and pyramid [Fig. 4(b)] Ge dots, and that for holes are displayed in the right-hand images. Figure 4(c) plots the distributions for a pyramid dot buried in a Si matrix. From Fig. 4 we see the following trend: In a buried dot, the electrons are localized just above the apex of the pyramid, as has been reported so far.[15] In contrast, the hole wave function is confined inside the dot in all three cases, causing the holes to be closer to the top of uncapped dots in Figs. 4(a) and 4(b). Finally, the lowest electron states for uncapped dots are located below the bottom of the dots, which more or less come close to the interface [left-hand images in Figs. 4(a) and 4(b)].

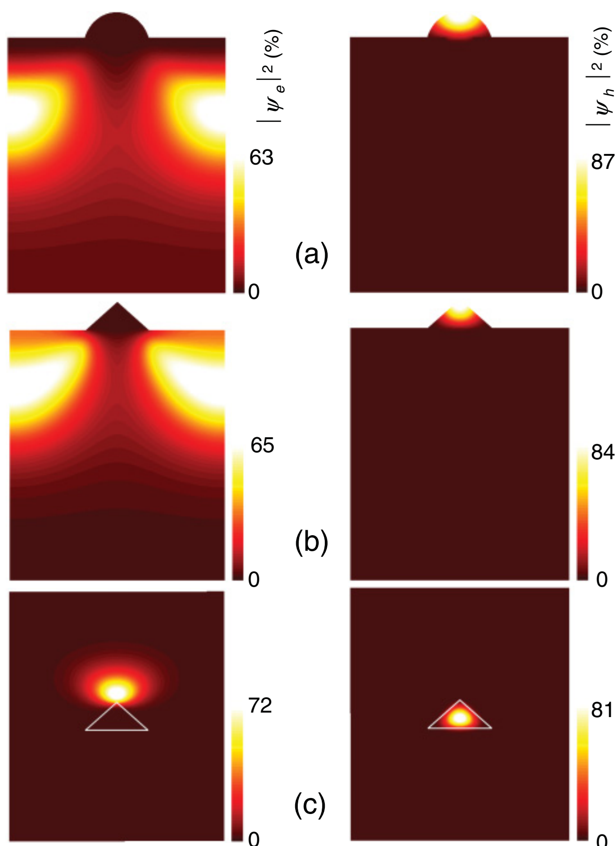

FIG. 4. (Color online) Probability density function $|\psi|^2$ profiles (24×28 nm^2 in size) for energy levels of the ground state corresponding to conduction band (left-hand side) and heavy-hole band (right-hand side) for (a) hemisphere uncapped Ge dot, epitaxially grown on oxidized Si surface [(a) in Fig. 2], (b) pyramid uncapped Ge dot grown on a bare Si surface [(c) in Fig. 2], and (c) pyramid Ge dot buried in a Si matrix. Base diameter in (a) and base side in (b), (c) are 7 nm, the dot heights are 2.5 nm in all cases, the thickness of the SiO_2 layer in (a) is 0.3 nm, and the interdot distance is 24 nm ($n_{QD} = 1.7 \times 10^{11}$ cm^{-2}).

Comparing Figs. 4(a) and 4(b), one sees how the qualitative trend comes about: The electron ground state can be squeezed deeper inside the Si substrate due to insertion of an intermediate ultrathin oxide layer, thus providing a greater distance for the separated electrons and holes.

In order to understand this trend in greater detail, Fig. 5 shows the electron localization depth as a function of the dot density for varying parameters of the dot. By inspection of curves 1 to 3 in Fig. 5, it is apparent that varying density of the dots is playing a major role; we see significant increases in electron localization depth for uncapped hemisphere QDs with decreasing n_{QD} in the range $\approx 10^{12}$ to 10^{10} cm^{-2} and decreases as the dot size increases from $D = 7$ nm (curve 1) to $D = 22$ nm (curve 3). In the plot, the variation of the dot density is limited to the values for the realistic cases given in Sec. II. It turns out that the depth is not very sensitive to Ge fraction x (circles and squares in Fig. 5). To test the dependence upon the aspect ratio, calculations are performed for varying AR (open and closed diamonds in Fig. 5), keeping other parameters the same, and for varying dot size (curves 2 and 3), keeping the aspect ratio fixed. From these, we can draw the conclusion that the localization depth is not significantly affected by varying the aspect ratio.

In marked contrast, the localization depth for an uncapped pyramid QD does not significantly change (by less than 1%) when taking into account a realistic density of QDs (curve 4 in Fig. 5). Our numerical solutions show that, similarly to an uncapped pyramid, the localization depth for a buried pyramid QD exhibits only a weak dependence on n_{QD} (curve 6 in Fig. 5). For buried hemisphere dots, the localization depth seems to increase only slightly with increase in the dot density from 10^{10} to 10^{12} cm^{-2} (curve 5 in Fig. 5), as opposed to the data for uncapped hemisphere QDs (curves 1 to 3). It is interesting to note that the depths for uncapped and buried pyramid QDs given by curves 4 and 6, respectively, are quite similar in magnitude, whereas the ones for hemisphere QDs (curves 1 and 5) are significantly different in both magnitude and dependence on n_{QD}. This is to be expected since a necked hemisphere shape, realized on oxidized surfaces, implies the strain situation under the dot is somewhat more complicated compared with that developed both above and under the dot deposited on an initially bare surface. Consequently, in the neighborhood of a small neck, even deeper inside the Si substrate, the electron density distribution clearly differs from that above the dot.

We therefore conclude that enhanced electron localization depths in the Si substrate and, consequently, greater electron-hole separation distances can be realized for uncapped hemisphere QDs with diameters smaller than 15–20 nm over a range of dot densities, which extends from 10^{10} to $(1–2)\times 10^{12}$ cm^{-2} in curves 1 and 2 of Fig. 5, in striking contrast to pyramid QDs (curves 4 and 6). Hence, under certain experimental circumstances, the effect may be considerably large, giving

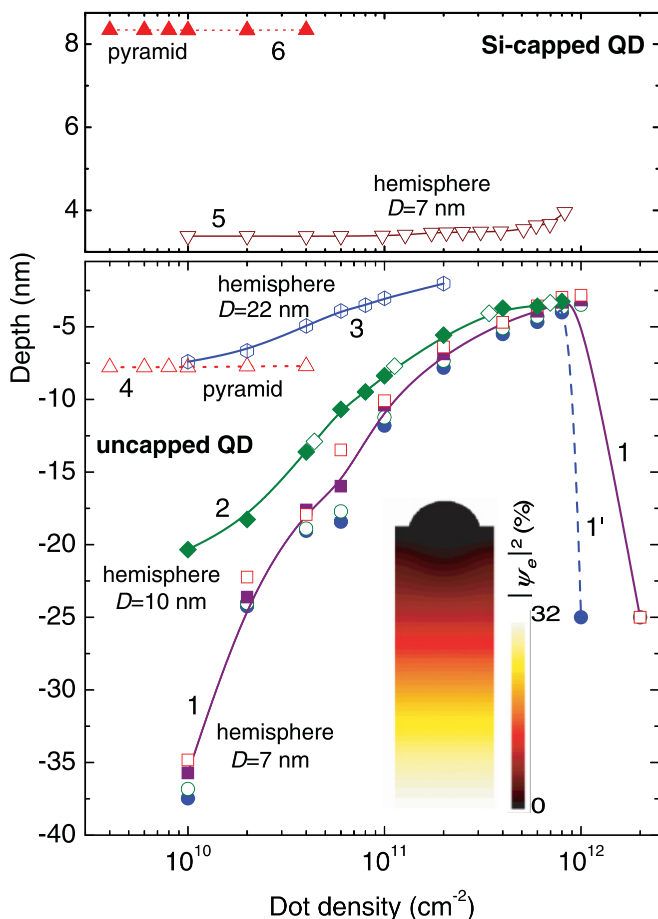

FIG. 5. (Color online) Electron localization depth (distance from the QD and substrate interface plane to the $|\psi|_e^2$ maxima in the left-side images of Fig. 4) as a function of the dot density for an uncapped (curves 1 to 4) and Si-capped (curves 5 and 6) Ge_xSi_{1-x} alloyed pyramid QD with a base length of 50 nm, height of 7 nm, $x = 0.7$ (curves 4 and 6), and hemisphere QDs with $D = 7$ nm, $H = 2.5$ nm (AR = 0.4), $d = 1$ nm (curve 1) for $x = 0.7$ (closed circles), 0.8 (open circles), 0.9 (closed squares), 1.0 (open squares); $D = 10$ nm, $H = 8$ nm (AR = 0.8, closed diamonds) and $H = 3.6$ nm (AR = 0.4, open diamonds), $d = 2$ nm, $x = 0.7$ (curve 2); $D = 22$ nm, $H = 18$ nm (AR = 0.4), $d = 2$ nm, $x = 0.7$ (curve 3); $D = 7$ nm, $H = 2.5$ nm (AR = 0.4), $d = 1$ nm, $x = 0.7$ (curve 5). Points are calculated data, curves 1 to 6 are drawn as a guide to the eye. Inset: $|\psi_e|^2$ profile (10×28 nm^2) for a hemisphere QD with $D = 7$ nm, $H = 2.5$ nm (AR = 0.4), $d = 1$ nm, $x = 0.7$, and $n_{QD} = 10^{12}$ cm^{-2}.

rise to the depths increasing from about 8 nm for a pyramid to 38 nm for a hemisphere dot in curves 4 and 1 of Fig. 5, respectively.

Going further through the numerical derivation of uncapped hemisphere QDs, we find that, as n_{QD} is increased to a value above (1–2) $\times 10^{12}$ cm^{-2}, the electron density eventually evolves into delocalized states (inset in Fig. 5). Comparison of curves 1 and 1′ in Fig. 5 shows that this effect is slightly sensitive to the value of x.

To interpret this, it is tempting to consider the strain-induced confinement potentials for electrons and holes. These potentials, taken along the z direction and intersecting the maxima of $|\psi_e|^2$ and $|\psi_h|^2$, are displayed in Fig. 6. It is seen

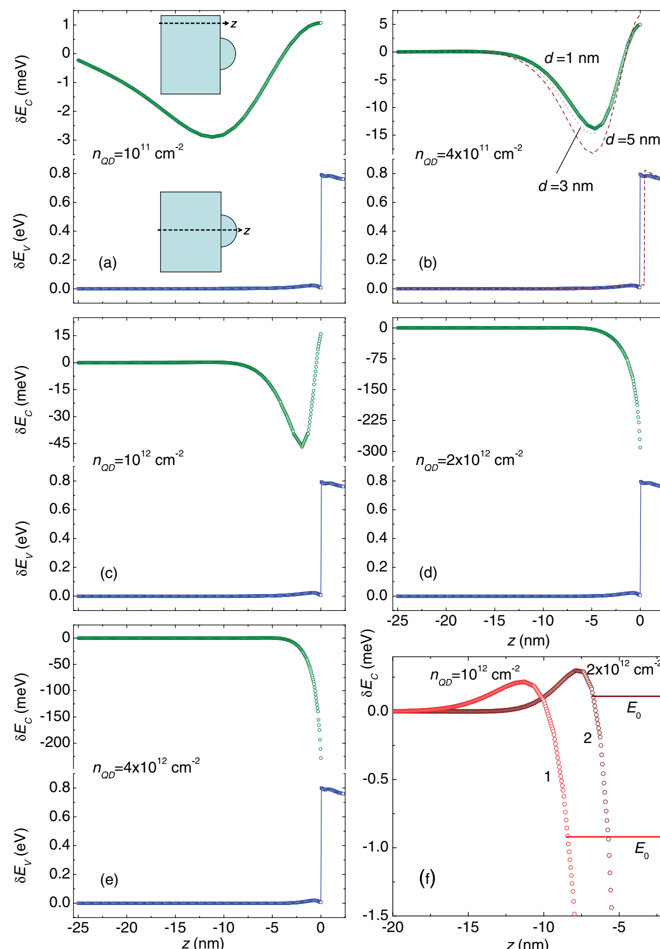

FIG. 6. (Color online) Distributions of the strain-induced shifts of the conduction (δE_C) and valence (δE_V) bands around an uncapped hemisphere Ge_xSi_{1-x} QD ($D = 7$ nm, $H = 2.5$ nm, $d = 1$ nm, $x = 0.7$) for linescans in the z direction intersecting the maximum of $|\psi_e|^2$ [left-hand image in Fig. 4(a)] for δE_C [upper inset in (a)], and going through the top of the dot for δE_V [lower inset in (a)] at $n_{QD} = 10^{11}$ (a), 4×10^{11} (b), 10^{12} (c), 2×10^{12} (d), and 4×10^{12} (e) cm^{-2}. Panel (f) enlarges the δE_C linescans at $n_{QD} = 10^{12}$ (curve 1) and 2×10^{12} (curve 2) cm^{-2} with the corresponding ground-state energies E_0. Effect of varying neck diameter d is illustrated by dotted and dashed curves in (b) computed for $d = 3$ and 5 nm, respectively.

that, in contrast with the valence-band potential (δE_V in Fig. 6), the one for electrons exhibits sizable changes in both shape and depth upon varying n_{QD} [δE_C in Figs. 6(a) to 6(e)]. The effect of varying neck diameter, illustrated by dotted and dashed curves in Fig. 6(b), shows that the shape and depth of δE_C do not vary by a large amount with d for a given diameter range.

Comparison of δE_C in Figs. 6(a) to 6(e) shows that the strain-modified confinement potential for electrons becomes deeper and narrower with increasing n_{QD}. This may open a bypass channel through which the electrons can flow from the ground state E_0 in the dot into the continuum states lying deeper inside the Si substrate. The flow will increase continuously with narrowing the potential, as the narrowing lifts E_0 up. To summarize this behavior, Fig. 6(f) plots two enlarged δE_C profiles and marks the corresponding ground-state energies E_0. One sees that, for n_{QD} ranged between

1×10^{12} and 2×10^{12} cm^{-2}, the E_0 level touches electron states in the continuum (at $z \leqslant -15$ nm), which empties the localized states in the dot by populating the continuum states. The existence of this crossover point for the energy levels seems to explain naturally the fact that the electron density becomes delocalized at n_{QD} greater than (1–2) $\times 10^{12}$ cm^{-2}, as pointed out above.

Thus far, we have not yet addressed the influence of the band bending at the Si/SiO$_2$ interface (i.e., the fixed oxide charge density Q_{ox} and the bulk doping level) on confinement of free charge carriers. To understand this, here we consider an oxidized p-type Si substrate with fixed bulk doping shown in the inset of Fig. 7. It is known that the Si/SiO$_2$ interface contains positive charges in the oxide with Q_{ox} ranging from about 10^{-9} to 10^{-7} C/cm^2,[74,75] which is balanced by an opposite space charge in a layer of width W underneath the interface (inset in Fig. 7). The charge distribution produces an electric field within the space charge region and a corresponding downward band bending at the silicon surface ($e\varphi_{sc}$ in the inset of Fig. 7, where e is the electron charge), following from Poisson equation. Assuming depletion, the induced Si charge density $-Q_{sc}$ consists of ionized acceptors in the space charge region $Q_{\mathrm{ox}} = |Q_{sc}| = eN_A W$, where N_A is the acceptor doping density. Then, the interface potential and the thickness of the depletion layer are[76]

$$\varphi_{sc} = \frac{Q_{\mathrm{ox}}^2}{2\varepsilon\varepsilon_0 e N_A} \quad (20)$$

and

$$W = \sqrt{\frac{2\varepsilon\varepsilon_0\varphi_{sc}}{eN_A}}, \quad (21)$$

respectively, where ε =11.9 (Ref. 77) is the dielectric function and ε_0 is the permittivity of free space. Taking $N_{\mathrm{ox}} = Q_{\mathrm{ox}}/e = 10^{10}$ cm^{-2} and $N_A = 1.3 \times 10^{15}$ cm^{-3} [for a wafer resistivity of 10 Ω cm (Ref. 78)], a minimum value of $W = N_{\mathrm{ox}}/N_A$ is about 100 nm, which extends well beyond the region of interest in Fig. 6.

Within this model, the effect of oxide charges is accounted for by adding the value of $e\varphi(z)$ in Eqs. (4) and (5). The potential φ as a function of distance z is obtained by integrating the one-dimensional Poisson equation from the substrate bulk toward the interface, which gives[76]

$$\left(\frac{d\varphi}{dz}\right)^2 = \left(\frac{2kT}{e}\right)^2 \left(\frac{ep_o\beta}{2\varepsilon\varepsilon_0}\right) F^2\left(\beta\varphi, \frac{n_i}{p_o}\right), \quad (22)$$

where k is the Boltzmann constant, T is the temperature, $\beta = e/kT$, p_o is the hole concentration in the bulk of the Si substrate, n_i is the intrinsic carrier concentration in the bulk, and

$$F^2\left(\beta\varphi, \frac{n_i}{p_o}\right) = (e^{-\beta\varphi} + \beta\varphi - 1) + \frac{n_i}{p_o}(e^{\beta\varphi} - \beta\varphi - 1). \quad (23)$$

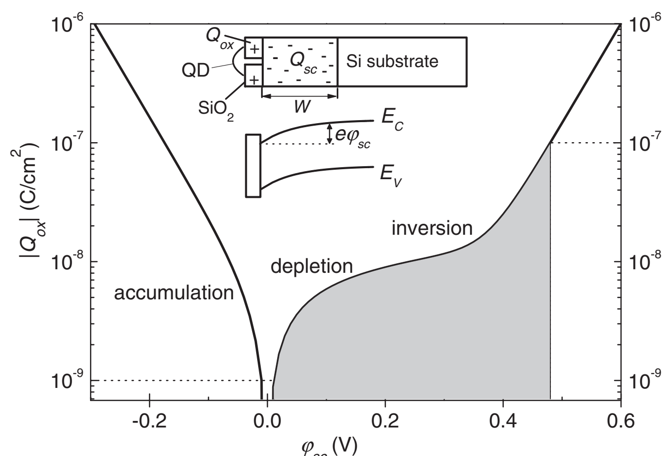

FIG. 7. Calculated Q_{ox} as a function of φ_{sc} at $p_o = N_A = 1.3\times10^{15}$ cm^{-3} and $n_i = 9.7 \times 10^9$ cm^{-3} (Ref. 78). Inset: cross section and band diagram of a Si/SiO$_2$ system showing the band bending $e\varphi_{sc}$ in the space charge region of width W.

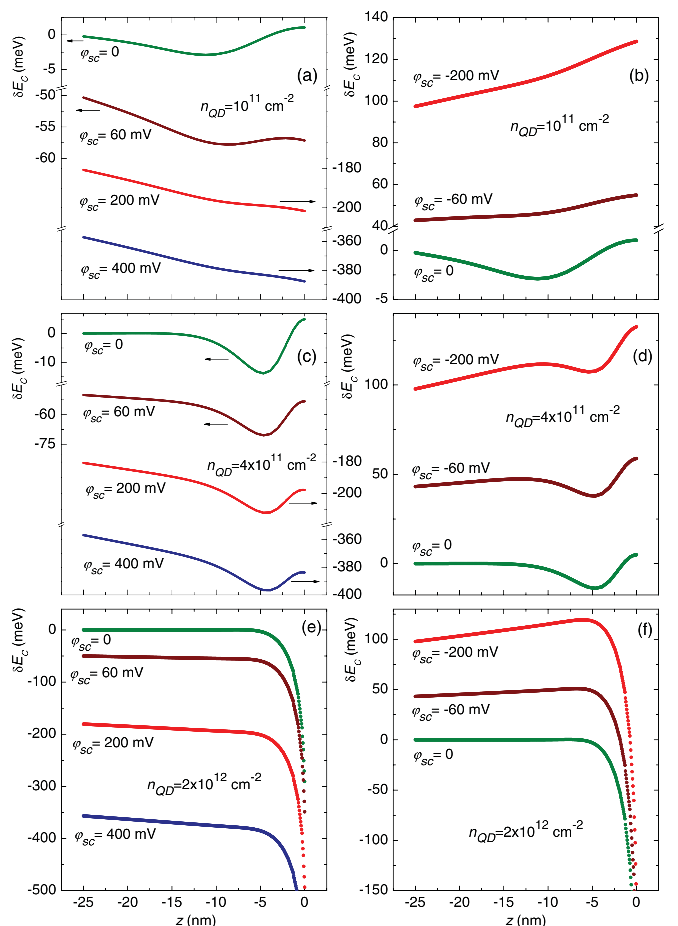

FIG. 8. (Color online) Distributions of the strain-induced shift of the conduction band (δE_C) at $n_{\mathrm{QD}} = 10^{11}$ [(a) and (b)], 4×10^{11} [(c) and (d)], and 2×10^{12} [(e) and (f)] cm^{-2} for positive (left-hand panels) and negative (right-hand panels) φ_{sc} ranging from 400 to -200 mV. The geometry that we use is shown in the upper inset of Fig. 6(a).

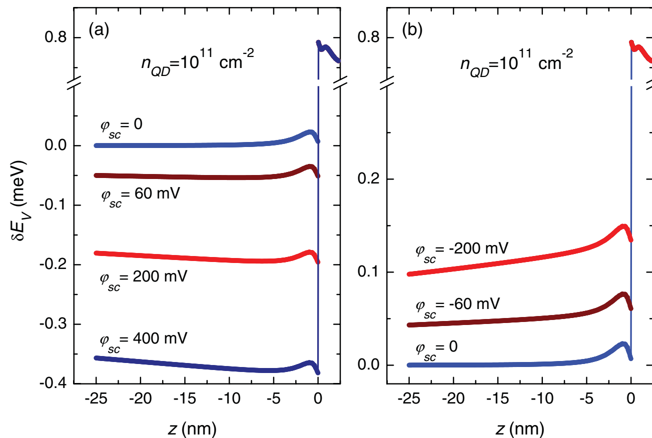

FIG. 9. (Color online) Distributions of the strain-induced shift of the valence band (δE_V) at $n_{\rm QD} = 10^{11}$ cm^{-2} for positive (a) and negative (b) φ_{sc} ranging from 400 to -200 mV. The geometry that we use is shown in the lower inset of Fig. 6(a).

Equation (22) is solved with the boundary condition, $\varphi(z = 0) = \varphi_{sc}$, where φ_{sc} is related to $Q_{\rm ox}$ as[76]

$$Q_{\rm ox} = \mp\sqrt{2\varepsilon\varepsilon_0 kTp_o}\,F\left(\beta\varphi_{sc}, \frac{n_i}{p_o}\right). \qquad (24)$$

The corresponding $Q_{\rm ox}$ versus φ_{sc} dependence, calculated for $p_o = N_A$, is shown in Fig. 7. The results demonstrate that $Q_{\rm ox}$ can be split into three charge contributions: accumulation, depletion, and inversion charge.[76] The hatched area shows the range of φ_{sc} (from 0 to 480 mV), which corresponds to reported values of $Q_{\rm ox}$ (dotted lines in Fig. 7) and is used to study the effect of the oxide charge on confinement of free charge carriers. For the purpose of comparison we will also discuss the consequences that follow from the negative oxide charge (for the values of φ_{sc} ranging from 0 to -200 mV).

To demonstrate the effect of the oxide charge on the strain-induced confinement potentials for electrons, we plot in Fig. 8 a series of δE_C curves computed at different φ_{sc}. As φ_{sc} is increased from 0 to +400 mV, the δE_C curves shift downward [Figs. 8(a), 8(c), and 8(e)]. In turn, decreasing φ_{sc} from 0 to -200 mV shifts the curves upward, as Figs. 8(b), 8(d), and 8(f) illustrate. Similar shifts are also observed for the valence-band potential shown in Fig. 9. This is clearly due to a downward and upward band bending induced by $Q_{\rm ox} > 0$ and $Q_{\rm ox} < 0$, respectively, which in turn cause significant curve shifts observed in Figs. 8 and 9.

By inspection of the curves in Fig. 8, it is also apparent that the higher $+\varphi_{sc}$ and lower $-\varphi_{sc}$ result in shallower confinement potentials on their right-hand sides [Figs. 8(a) and 8(c)] and left-hand sides [Figs. 8(b) and 8(d)], respectively. This, again, is due to either a downward ($+\varphi_{sc}$) or upward ($-\varphi_{sc}$) band bending at the Si/SiO_2 interface. Consequently, a positive oxide charge $+Q_{\rm ox}$ would cause confined electrons to move toward the Si/SiO_2 interface. In contrast, the electrons are swept out from the confinement region deeper into the substrate when the negative charge $-Q_{\rm ox}$ is formed in the oxide. The trend with varying $n_{\rm QD}$ is also obvious in Fig. 8: At moderately low density of the dots ($n_{\rm QD} \approx 10^{11}$ cm^{-2}), the confinement potential minimum is clearly destroyed if the oxide charge $Q_{\rm ox}$ is greater than $\approx 4 \times 10^{-9}$ C/cm^2 [$|\varphi_{sc}|$ exceeds a value of $\approx$60 mV in Figs. 8(a) and 8(b)]. However, it turns out that the confinement potential is much less affected by the oxide charge at higher QD densities (greater than $\approx 5 \times 10^{11}$ cm^{-2}). This is best seen in Figs. 8(e) and 8(f).

V. CONCLUSIONS

In conclusion, we have studied electronic properties of Ge_xSi_{1-x} quantum dots grown on oxidized Si surfaces. An account of strain distributions and electron localization depths in the strain-induced potential has been given in the framework of the continuum elasticity theory. Using realistic parameters and conditions for uncapped and buried dots, it is found that uncapped hemisphere dots grown on the Si surface with an intermediate ultrathin oxide layer offer advantageous electron-hole separation distances with respect to square-based pyramid dots grown directly on Si. For an uncapped hemisphere dot, the electron ground state can be squeezed deeper inside the Si substrate compared with the case of a pyramid dot, thus providing a greater distance for the separated electrons and holes. The resulting electron localization depth for a hemisphere dot is up to five times greater than that for a pyramid dot. The effect is very sensitive to the dot density and size, whereas the localization depth is not significantly affected by Ge fraction x in Ge_xSi_{1-x} alloyed dots and by changing the aspect ratio of the dot. Model calculations have been extended further to investigate the relationship between the electron confinement potential in Si and the Si/SiO_2 interface band bending induced by oxide charges $Q_{\rm ox}$. For a 10-Ω cm p-type Si wafer, it has been found that $Q_{\rm ox}$ should be moderately low ($\sim 10^{-9}$ C/cm^2) in order to avoid large perturbations of the confinement potential if the dot density is smaller than $n_{\rm QD} \approx 4\times 10^{11}$ cm^{-2}. We expect that the oxide charge with densities ranging from about 10^{-9} to 10^{-7} C/cm^2 does not play a significant role in determining the modified electronic properties in confinement potentials at higher $n_{\rm QD}$. We believe that the results presented here are applicable to functional devices utilizing separated electrons and holes, including photovoltaic devices, spin transistors, and quantum computing components.

ACKNOWLEDGMENTS

O.K. wishes to acknowledge the financial support of the Universitat de València through UV-ESTPC-10-24365. A.C. would like to thank the Ministry of Science and Innovation of Spain (Grant No. CSD2010-00044 of the programme Consolider Ingenio 2010).

*Permanent address: Department of Physics, Taras Shevchenko Kyiv National University, Kyiv 01601, Ukraine.

[1] Z. Liu, J. Wu, W. Duan, M. G. Lagally, and F. Liu, Phys. Rev. Lett. **105**, 016802 (2010).
[2] F. Boxberg and J. Tulkki, Rep. Prog. Phys. **70**, 1425 (2007).
[3] G. Abstreiter, H. Brugger, T. Wolf, H. Jorke, and H. J. Herzog, Phys. Rev. Lett. **54**, 2441 (1985).
[4] O. G. Schmidt and K. Eberl, Phys. Rev. B **61**, 13721 (2000).

[5]O. G. Schmidt, K. Eberl, and Y. Rau, Phys. Rev. B **62**, 16715 (2000).
[6]C. Euaruksakul, F. Chen, B. Tanto, C. S. Ritz, D. M. Paskiewicz, F. J. Himpsel, D. E. Savage, Z. Liu, Y. Yao, F. Liu, and M. G. Lagally, Phys. Rev. B **80**, 115323 (2009).
[7]F. Schäffler, Semicond. Sci. Technol. **12**, 1515 (1997).
[8]K. Rim, J. L. Hoyt, and J. F. Gibbons, IEEE Trans. Electron Devices **47**, 1406 (2000).
[9]A. Alguno, N. Usami, T. Ujihara, K. Fujiwara, G. Sazaki, K. Nakajima, and Y. Shiraki, Appl. Phys. Lett. **63**, 1258 (2003).
[10]R. Oshima, A. Takata, and Y. Okada, Appl. Phys. Lett. **93**, 083111 (2008).
[11]J. D. Cressler and G. Niu, *Silicon-Germanium Heterojunction Bipolar Transistors* (Artech House, Norwood, 2003).
[12]S. Tong, J. L. Liu, J. Wang, and K. L. Wang, Appl. Phys. Lett. **80**, 1189 (2002).
[13]B. E. Kane, Nature (London) **393**, 133 (1998).
[14]S. Goswami, K. A. Slinker, M. Friesen, L. M. McGuire, J. L. Truitt, C. Tahan, L. J. Klein, J. O. Chu, P. M. Mooney, D. W. van der Weide, R. Joynt, S. N. Coppersmith, and M. A. Eriksson, Nat. Phys. **3**, 41 (2007).
[15]R. O. Rezaev, S. Kiravittaya, V. M. Fomin, A. Rastelli, and O. G. Schmidt, Phys. Rev. B **82**, 153306 (2010).
[16]G. Katsaros, P. Spathis, M. Stoffel, F. Fournel, M. Mongillo, V. Bouchiat, F. Lefloch, A. Rastelli, O. G. Schmidt, and S. De Franceschi, Nat. Nanotechnol. **5**, 458 (2010).
[17]V. Jovanović, C. Biasotto, L. K. Nanver, J. Moers, D. Grützmacher, J. Gerharz, G. Mussler, J. van der Cingel, J. J. Zhang, G. Bauer, O. G. Schmidt, and L. Miglio, IEEE Electron Device Lett. **31**, 1083 (2010).
[18]A. A. Shklyaev, M. Shibata, and M. Ichikawa, Phys. Rev. B **62**, 1540 (2000).
[19]A. V. Kolobov, A. A. Shklyaev, H. Oyanagi, P. Fons, S. Yamasaki, and M. Ichikawa, Appl. Phys. Lett. **78**, 2563 (2001).
[20]A. A. Shklyaev and M. Ichikawa, Surf. Sci. **514**, 19 (2002).
[21]A. Kanjilal, J. Hansen, P. Gaiduk, A. N. Larsen, P. Normand, P. Dimitrakis, D. Tsoukalas, N. Cherkashin, and A. Claverie, Appl. Phys. A **81**, 363 (2005).
[22]A. Konchenko, Y. Nakayama, I. Matsuda, S. Hasegawa, Y. Nakamura, and M. Ichikawa, Phys. Rev. B **73**, 113311 (2006).
[23]L. Zhang, H. Ye, Y. R. Huangfu, C. Zhang, and X. Liu, Appl. Surf. Sci. **256**, 768 (2009).
[24]Y. Nakamura, K. Watanabe, Y. Fukuzawa, and M. Ichikawa, Appl. Phys. Lett. **87**, 133119 (2005).
[25]A. A. Shklyaev, S. Nobuki, S. Uchida, Y. Nakamura, and M. Ichikawa, Appl. Phys. Lett. **88**, 121919 (2006).
[26]H. T. Johnson, L. B. Freund, C. D. Akyuz, and A. Zaslavsky, J. Appl. Phys. **84**, 3714 (1998).
[27]J. Grenzer, U. Zeimer, S. A. Grigorian, S. Feranchuk, U. Pietsch, J. Fricke, H. Kissel, A. Knauer, and M. Weyers, Phys. Rev. B **69**, 125316 (2004).
[28]A. D. Andreev, J. R. Downes, D. A. Faux, and E. P. O'Reilly, J. Appl. Phys. **86**, 297 (1999).
[29]A. D. Andreev and E. P. O'Reilly, Nanotechnology **11**, 256 (2000).
[30]J. H. Davies, J. Appl. Phys. **84**, 1358 (1998).
[31]E. Pan, J. Appl. Phys. **91**, 3785 (2002).
[32]E. Pan, J. Appl. Phys. **91**, 6379 (2002).
[33]E. Melezhik and O. Korotchenkov, J. Appl. Phys. **105**, 023525 (2009).
[34]G. Bastard, *Wave Mechanics Applied to Semiconductor Heterostructures* (Les Editions de Physique, Les Ulis, 1988).
[35]D. Rideau, M. Feraille, L. Ciampolini, M. Minondo, C. Tavernier, H. Jaouen, and A. Ghetti, Phys. Rev. B **74**, 195208 (2006).
[36]L.-W. Wang and A. Zunger, Phys. Rev. B **59**, 15806 (1999).
[37]C. Delerue and M. Lannoo, *Nanostructures: Theory and Modelling* (Springer, New York, 2004).
[38]Y. M. Niquet, D. Rideau, C. Tavernier, H. Jaouen, and X. Blase, Phys. Rev. B **79**, 245201 (2009).
[39]Y. Nakamura, Y. Nagadomi, K. Sugie, N. Miyata, and M. Ichikawa, J. Appl. Phys. **95**, 5014 (2004).
[40]T.-S. Yoon, Z. Zhao, J. Liu, Y.-H. Xie, D. Y. Ryu, T. P. Russell, H.-M. Kim, and K.-B. Kim, Appl. Phys. Lett. **89**, 063107 (2006).
[41]T.-S. Yoon, H.-M. Kim, K.-B. Kim, D. Y. Ryu, T. P. Russell, Z. Zhao, J. Liu, and Y.-H. Xie, J. Appl. Phys. **102**, 104306 (2007).
[42]Y. Nakamura, A. Murayama, R. Watanabe, T. Iyoda, and M. Ichikawa, Nanotechnology **21**, 095305 (2010).
[43]G. Medeiros-Ribeiro, A. M. Bratkovski, T. I. Kamins, D. A. A. Ohlberg, and R. S. Williams, Science **279**, 353 (1998).
[44]J.-M. Baribeau, X. Wu, N. L. Rowell, and D. J. Lockwood, J. Phys.: Condens. Matter **18**, R139 (2006).
[45]T. Wiebach, M. Schmidbauer, M. Hanke, H. Raidt, R. Kohler, and H. Wawra, Phys. Rev. B **61**, 5571 (2000).
[46]I. Kegel, T. H. Metzger, A. Lorke, J. Peisl, J. Stangl, G. Bauer, K. Nordlund, W. V. Schoenfeld, and P. M. Petroff, Phys. Rev. B **63**, 035318 (2001).
[47]T. U. Schülli, J. Stangl, Z. Zhong, R. T. Lechner, M. Sztucki, T. H. Metzger, and G. Bauer, Phys. Rev. Lett. **90**, 066105 (2003).
[48]A. Hesse, J. Stangl, V. Holý, T. Roch, G. Bauer, O. G. Schmidt, U. Denker, and B. Struth, Phys. Rev. B **66**, 085321 (2002).
[49]M. S. Leite, A. Malachias, S. W. Kycia, T. I. Kamins, R. S. Williams, and G. Medeiros-Ribeiro, Phys. Rev. Lett. **100**, 226101 (2008).
[50]D. Dutartre, G. Brémond, A. Souifi, and T. Benyattou, Phys. Rev. B **44**, 11525 (1991).
[51]C. Georgi, M. Hecker, and E. Zschech, J. Appl. Phys. **101**, 123104 (2007).
[52]D. E. Aspnes and A. A. Studna, Phys. Rev. B **27**, 985 (1983).
[53]P. A. Temple and C. E. Hathaway, Phys. Rev. B **7**, 3685 (1973).
[54]A. V. Kolobov, J. Appl. Phys. **87**, 2926 (2000).
[55]F. Cerdeira, A. Pinczuk, J. C. Bean, B. Batlogg, and B. A. Wilson, Appl. Phys. Lett. **45**, 1138 (1984).
[56]D. J. Lockwood and J. M. Baribeau, Phys. Rev. B **45**, 8565 (1992).
[57]D. W. Feldman, M. Ashkin, and H. Parker Jr., Phys. Rev. Lett. **17**, 1209 (1966).
[58]M. A. Renucci, J. B. Renucci, and M. Cardona, in *Light Scattering in Solids*, edited by M. Balkanski (Flammarion, Paris, 1971), p. 326.
[59]J. S. Lannin, Phys. Rev. B **16**, 1510 (1977).
[60]T. P. Pearsall, F. H. Pollak, J. C. Bean, and R. Hull, Phys. Rev. B **33**, 6821 (1986).
[61]S. H. Kwok, P. Y. Yu, C. H. Tung, Y. H. Zhang, M. F. Li, C. S. Peng, and J. M. Zhou, Phys. Rev. B **59**, 4980 (1999).
[62]M. I. Alonso and K. Winer, Phys. Rev. B **39**, 10056 (1989).
[63]D. J. Lockwood, K. Rajan, E. W. Fenton, J.-M. Baribeau, and M. W. Denhoff, Solid State Commun. **61**, 465 (1987).
[64]M. I. Alonso, M. de la Calle, J. O. Ossó, M. Garriga, and A. R. Goñi, J. Appl. Phys. **98**, 033530 (2005).
[65]P. H. Tan, K. Brunner, D. Bougeard, and G. Abstreiter, Phys. Rev. B **68**, 125302 (2003).
[66]J. H. Lin, H. B. Yang, J. Qin, B. Zhang, Y. L. Fan, X. J. Yang, and Z. M. Jiang, J. Appl. Phys. **101**, 083528 (2007).
[67]J. Nye, *Physical Properties of Crystals* (Clarendon, Oxford, 1985).

[68]O. Zienkiewicz and R. Taylor, *The Finite Element Method* (McGraw-Hill, London, 1989), Vol. 1.
[69]E. Polizzi, Phys. Rev. B **79**, 115112 (2009).
[70]C. G. Van de Walle, Phys. Rev. B **39**, 1871 (1989).
[71]B. A. Auld, *Acoustic Fields and Waves in Solids* (Wiley, New York, 1973).
[72]M. L. Lee and E. A. Fitzgerald, J. Appl. Phys. **97**, 011101 (2005).
[73]M. I. Vexler, S. E. Tyaginov, and A. F. Shulekin, Semiconductors **40**, 491 (2006).
[74]K. Yasutake, Z. Cheng, S. K. Pang, and A. Rohatgi, J. Appl. Phys. **75**, 2048 (1994).
[75]A. W. Stephens, A. G. Aberle, and M. A. Green, J. Appl. Phys. **76**, 363 (1994).
[76]S. M. Sze, *Physics of Semiconductor Devices* (Wiley, New York, 1981).
[77]R. Poerschke and O. Madelung, *Data in Science and Technology: Semiconductors* (Springer, Berlin, 1991).
[78]D. K. Schroder, *Semiconductor Material and Device Characterization* (Wiley, New Jersey, 2006).